Rock Mech Rock Eng (2012) 45:837–849
DOI 10.1007/s00603-011-0180-3

ORIGINAL PAPER

A Study of Optimal Rock-Cutting Conditions for Hard Rock TBM Using the Discrete Element Method

T. Moon · J. Oh

Received: 13 February 2011 / Accepted: 30 August 2011 / Published online: 20 September 2011

Abstract The efficiency of TBM performance affected by the specific *s/p* (*s*: spacing and *p*: penetration) ratio of the disc cutter is a research issue in demand. This article presents a multi-indentation simulation using discrete element method (DEM) analysis to study the optimal rock-cutting phenomena in terms of the interaction of the *s/p* ratio with intact rock properties. The multi-indentation simulation attempts to represent a linear cutting machine (LCM) test, which is a full-scale test for evaluating the optimal rock-cutting condition and measuring required reaction forces based on the intact rock condition in general practice. A governing equation relating mechanical rock properties with geometric characteristics for the optimal rock-cutting condition is derived by the numerical simulation, and its performance is evaluated with the result of the laboratory LCM tests. The results of simulations and real LCM tests show that the effective rock-cutting condition corresponding to the minimum specific energy can be estimated by an optimized *s/p* ratio, which, in turn, is linearly proportional to the square of the material brittleness, B^2, and cutter tip width, t (i.e., $s/p = cB^2t$, where c is coefficient). The limitation of the numerical simulation associated with the sample preparation is also discussed.

Keywords LCM · DEM · Multi-indentation · *s/p* ratio · TBM · Brittleness

---

T. Moon · J. Oh (✉)
PB Geotechnical and Tunneling, Parsons Brinckerhoff Inc.,
One Penn Plaza, New York, NY 10119, USA
e-mail: ohjo@pbworld.com

List of symbols

A	Contact area of indenter
A_c	Total crack areas
α	Internal crack angle
B	Brittleness
c	Constant coefficient
$\tilde{D}$	Average diameter of assemblage
δ	Arbitrary position angle
E	Young's modulus
E'	Young's modulus for plane strain
F_c	Crack-related force
F_t	Peak load of indenter
G_{IC}	Strain energy release rate for mode I
K_{IC}	Fracture toughness for mode I
K_n	Normal stiffness
k_s	Shear stiffness
μ	Friction coefficient
$\mathbf{v}$	Poisson's ratio
p	Penetration of disc cutter
θ	Contact angle between disc and rock sample
$\dot{\theta}$	Angular velocity
H	Material hardness
L	Unit length
N_c	Number of debonded particles
r_c	Chipping radius
s	Spacing of disc cutter
σ_c	Compressive strength
σ_t	Tensile strength
t	Tip width of disc cutter
T_n	Normal bonding
T_s	Shear bonding
τ	Shear strength
U_t	Total energy
U_s	Strain energy

U_f	Friction energy
v_a	Tangential velocity
v_{ax}	x Component of tangential velocity
v_{ay}	y Component of tangential velocity

1 Introduction

With rapid growth of the use of tunnel boring machines (TBMs), extensive research has been conducted to achieve a more comprehensive understanding of various facets of TBM technology. TBM performance and efficiency are heavily dependent on the rock properties, such as strength and stiffness, as well as the geometric characteristics of machine, such as disc cutter array, disc diameter, and tip width. Roxborough and Phillips (1975) observed the influence of the spacing, s, and penetration, p, of a disc cutter versus the magnitude of cutting forces and specific energy from a liner cutting machine (LCM) test, which is a full-scale test for evaluating the optimal rock-cutting condition and measuring reaction forces required. The specific energy is calculated by requirement energy per unit volume of rock chipping (Teale 1965). Roxborough and Phillips (1975) also suggested that the optimized s/p ratio is correlated with the ratio of compressive strength, σ_c, to shear strength, τ, of the rock. Snowdon et al. (1982) from laboratory experiments showed that there is a constant s/p ratio for minimum specific energy. However, they explained that there is no simple relation between the optimized s/p ratio and any combination of the rock strength parameters. Rostami and Ozdemir (1993) postulated that there are three different chipping patterns in terms of specific spacings, and also there is an optimal rock-cutting spacing corresponding to an effective rock-cutting condition. Most recently, Gertsch et al. (2007) conducted a series of full-scale laboratory disc-cutting tests, shown in Fig. 1, and showed that a certain disc cutter spacing is close to the optimum specific energy in hard, brittle, crystalline rock.

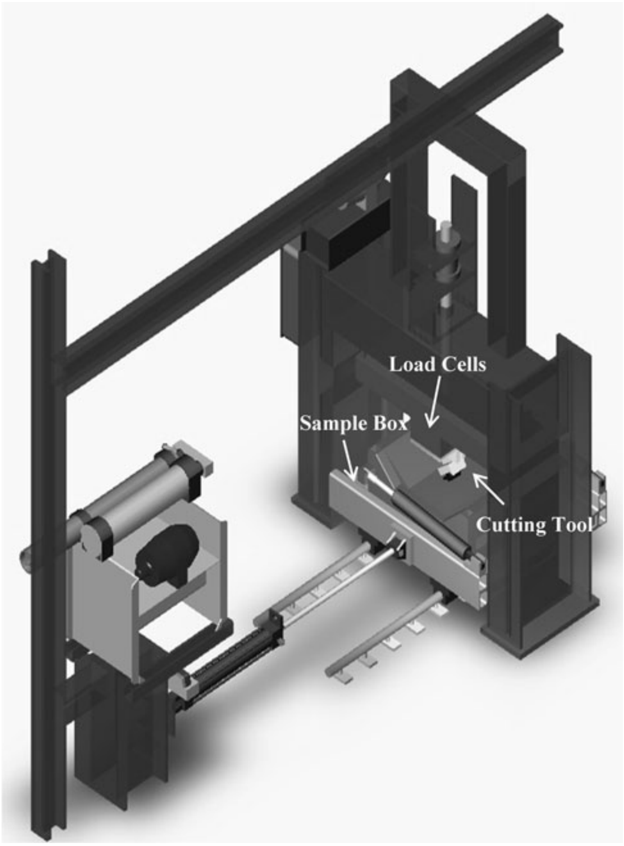

Fig. 1 Schematic view of the linear cutting machine (LCM) of the Colorado School of Mines (CSM)

Lawn and Swain (1975) and Swain and Lawn (1976) observed and analyzed two main types of crack formation from point indentations in brittle solids; after the creation of the irreversible crush zone under the indenter, median vents are formed during loading conditions, and then lateral vents under tensile failure mode are formed during unloading conditions, spreading sideways toward the specimen surface. Even though the rock fragmentation process over the disc cutter occurs by more complicated interactions among normal, rolling, and side forces, the theoretical and experimental studies on rock fragmentation using the indentation tests are generally adaptable to understanding the rock-chipping mechanism of the disc cutter since the rock fragmentation of the disc cutter is also a process of repeated loading and unloading induced by the circular shape of the disc cutter with continuous moving.

Numerical methods to provide better understanding of rock fragmentation processes have been employed by several researchers. Cook et al. (1984) examined the effects of indenter size and confining stress on the rock indentation test and compared it with numerical simulation based on the finite element method (FEM). Liu et al. (2002) performed numerical simulation, R-T^{2D}, of the rock fragmentation process using single or simultaneous multi-indenters under constant displacement control with various high confining stresses. For the indentation simulations, high confining stress was required to generate rock chipping. Gong et al. (2006a, b) performed single and simultaneous multi-indentation numerical simulations to investigate joint spacing effects using the discrete element method (DEM) based on the fixed boundary condition and load-controlled indenters.

The aforementioned numerical studies of the single or multi-indentation rock-cutting tests well presented the considerable rock-chipping process and comparable crack patterns in accordance with laboratory tests. However, the loading and boundary conditions of the numerical studies did not fully represent the LCM test. The LCM test is in general carried out under a constant penetration depth with sequential multi-cutting paths with application of no additional confining stress on the rock sample. The rock sample of the LCM test is also preconditioned by several cuts before data acquisition to ensure that the rock surface reaches the same degree of steady state as found on a TBM tunnel face (Gertsch et al. 2007).

Cho et al. (2010) performed a three-dimensional dynamic numerical analysis based on the FEM for simulating the LCM test under non-reflective boundary conditions with sequential multi-cutting paths to represent more realistic boundary conditions and the process of the LCM test. For illustrating crack and chipping formation on the modeling, a numerical elimination technique triggered by pre-determined tensile strength was employed.

While the relation of cutting forces or specific energy to the configuration of the disc cutter may be understood to some extent, the interaction of these with rock properties has not been fully defined. Many performance prediction models have proposed relating the failure mechanism with rock strength parameters, such as compressive strength, tensile strength or shear strength. Because of the complex nature of the cutting process, however, the failure mechanism cannot be fully explained by just one of these parameters.

This article illustrates the rock-chipping process on the basis of the fracture mechanics and implies the most important mechanical parameters for optimal rock-cutting conditions using a particle flow code (PFC2D 1999). The PFC2D is a discontinuum code and allows crack formation and its propagation through the system (Potyondy and Cundall 2004). Initially, a synthetic rock material is calibrated by using uniaxial compressive strength (UCS) and Brazilian strength (BTS) tests. Then, a series of the sequential multi-indentation tests to represent the laboratory LCM test is carried out under similar loading and boundary conditions as in the LCM test. Furthermore, a parametric study is implemented using various rock properties under the various rock-cutting conditions in order to develop a governing equation of the optimal rock-cutting condition. The governing equation is then validated with the result of the laboratory LCM tests. It is noted that an anisotropic effect due to the presence of defects and/or joints of rock specimens is beyond the scope of this study.

2 Model Preparation with Calibration

A two-dimensional bonded particle model (BPM) detailed by Potyondy and Cundall (2004) has been employed with randomly sized particles using the distinct element code, PFC2D. The particles are assumed to be rigid, and the behavior of the assembly is characterized by the linear stiffness model, the contact-bond model, and the slip model. The linear stiffness model provides a linear relationship between contact force and relative displacement. The contact-bond model controls strength features of a synthetic material using the bonding strength. The slip model allows for slip between two contacting particles.

An attempt is made to numerically create a sample of Idaho basalt. The known macroscopic properties of Idaho basalt measured from the laboratory tests such as Young's modulus, E, Poisson's ratio, υ, compressive strength and tensile strength, σ_t, should be captured through the interaction of the microscopic properties of particles that have normal bonding strength, T_n, shear bonding strength, T_s, normal stiffness, K_n, shear stiffness, k_s, and friction coefficient, μ.

Unfortunately, there is no straightforward method currently available to calibrate the synthetic rock material from the micro properties. However, several researchers have attempted to improve and simplify the calibration procedure. Moon et al. (2007) evaluated the relationship between micro and macro properties in PFC2D on synthetic rock by simulating UCS, BTS, and notched Brazilian tests. Yoon (2007) provided a new approach to calculate proper micro parameters for model generation by using the Plackett-Burman (PB) design method and Central Composite Design (CCD) method, including an optimization process. For the current study, the same calibration process done by Moon et al. (2007) is applied in the numerical model by using UCS and BTS tests as shown in Fig. 2.

Potyondy and Cundall (2004) demonstrated the scale effect of the particle is not significant in rock modeling under compressive loading conditions. The number of particles, i.e., the size of particles for the current model, is decided on the effective model run times and model size after evaluating the various scaled models. Thereafter, 9,156 and 3,574 particles are used to make up the USC and BTS samples, respectively. The average radius of particles is 0.39 mm. The radius of the particles ranges from 0.3 mm to 0.49 mm with normal distribution. The synthetic specimen is created by the technique of expansion elimination of particles described by Potyondy et al. (1996). This technique is available to control both the size distribution and packing density at the same time.

Table 1 presents micro and macro properties of the synthetic sample and experimental results of Idaho basalt. As shown in Table 1, the simulation and experimental results are comparable to each other except the values of the compressive strength, in which the values of the synthetic samples are smaller than that of laboratory test. Further discussion on the discrepancy in compressive strengths between synthetic and natural samples is given in a later section.

After calibrating the Idaho basalt, the strain energy release rate, G_{IC}, to estimate fracture resistance is calculated by an energy balance approach on the basis of the Griffith theory

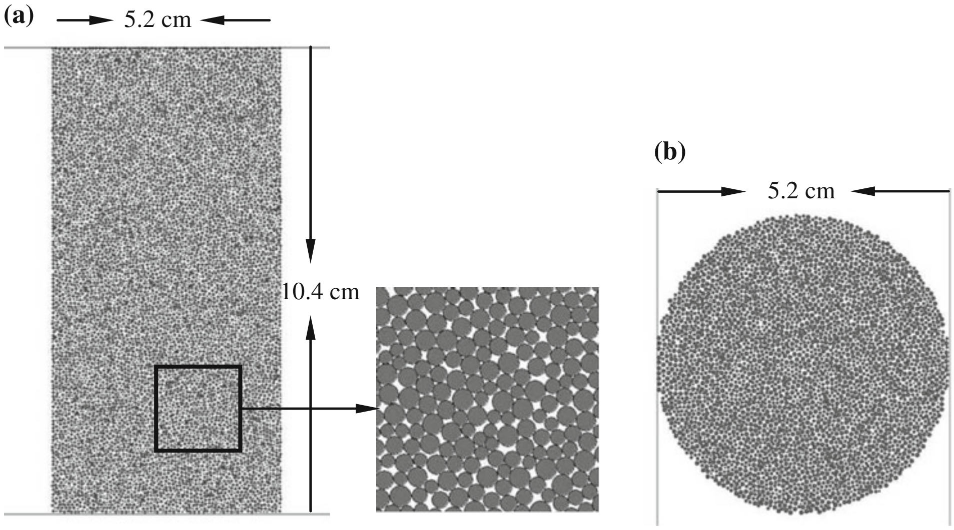

Fig. 2 Two-dimensional simulated disk assemblies for **a** UCS (9,156 particles; 10.4 cm height with 5.2 cm width) and **b** BTS sample (3,574 particles and 5.2 cm diameter)

Table 1 Micro and macro properties for synthetic samples in DEM

Micro properties (PFC2D)		Macro properties (PFC2D)		Macro properties (laboratory)	
T_n	0.18 MN/m	σ_c	28.4 MPa	σ_c	35–63 MPa
T_s	0.32 MN/m	σ_t	6.6 MPa	σ_t	1.7–8.4 MPa
K_n	30 GN/m^2	E	9.66 GPa	E	9 GPa
k_s/K_n	0.25	v	0.21	v	0.22
Grain radius mean	0.39 mm	K_{IC}	0.81 MPa$\sqrt{\text{m}}$	K_{IC}	0.88 MPa$\sqrt{\text{m}}$

(1921). According to Griffith, a crack can be extended when the theoretical strength of the material is reached at the crack tip. The source of energy for crack propagation is the strain energy released as the crack extends. The measure of G_{IC} on the DEM based upon the energy balance approach (Moon et al. 2007) is obtained by the derivative of crack energy, U_c, in terms of crack area, A_c, as follows:

$$\frac{dU_c}{dA_c} = \frac{d(U_t - U_s)}{dA_c} = G_{IC} \tag{1}$$

The crack energy, U_c is

$$U_c = U_t - U_s \tag{2}$$

where U_t is a total accumulated work done by the moving walls on the assembly, and U_s is a strain energy computed by the amount of overlap at all contacts between particles in the assembly. A_c is defined as

$$A_c = N_c\tilde{D}L \tag{3}$$

where N_c is a number of debonded particles, and $\tilde{D}$ is an average diameter of the assemblage. L is a unit depth (1 m). It is assumed that the unit crack length is approximately equivalent to $\tilde{D}$ (Huang 1999). The measure of G_{IC} in Eq. 1 is converted to fracture toughness, K_{IC}, shown in Table 1 on the basis of the linear fracture mechanics (LEFM) as the following relation:

$$G_{IC} = \frac{K_{IC}^2}{E'} \tag{4}$$

where E' is plain strain Young's modulus. The measure of K_{IC} from the numerical simulation and Eq. 4, and the notched Brazilian test proposed by Yarema and Krestin (1966) have good agreement, as shown in Table 1.

3 Fragmentation Process Induced by a Multi-Indentation Test

A multi-indentation simulation using the synthetic rock material is performed to represent LCM test. The dimension of the rock sample composed of 23,513 particles is 20 cm wide and 7 cm tall, as shown in Fig. 3. The size of the rock sample is determined by considering both minimal boundary effects and effective model run time. Fixed boundary conditions for the sides and bottom of the walls are applied with no confining stresses.

Figure 4 shows the side and front views of the disc cutter to present each velocity component of the disc cutter. A loading condition of the disc cutting over the two-dimensional simulation is varied in terms of a contact point between disc cutter and rock sample, which is as a function of the cutter radius, R_c, and the constant transversal velocity of the disc cutter, v_t. The tangential velocity, v_a, is calculated by the relationship between the transversal velocity, penetration depth and cutter radius.

$$v_a = \frac{v_t \theta R_c}{R_c \sin\theta} = \frac{v_t \theta}{\sin\theta} \tag{5}$$

where θ is the contact angle between the disc and rock sample at the full penetration depth. The tangential velocity of the y component at any contact point is given by

$$v_{a_y} = v_a \sin\delta \tag{6}$$

where δ is the angle of an arbitrary contact point between cutter and rock sample. Equation 6 implies the velocity of the indenter is gradually decreased as the penetration depth increases. In this study, 8.4 mm of the cutter tip width, 0.254 m/s of the translational velocity, 4 mm of the penetration depth and 12.7 cm of the cutter diameter are used for representing the mini disc cutter (5 inches).

Figures 5 and 6 show a series of snapshots of the formation of crack systems and internal reaction forces. At the very beginning stage of the indentation test, the specimen deforms elastically. A highly stressed zone develops under the indenter, as shown in Fig. 6a. Higher reaction forces correspond to the relatively thicker lines. The compressive and tensile modes are implied by gray and black colors, respectively. The compressive force shows a radiating fan-shaped distribution, and the tensile force shows an outward circular propagation that is approximately perpendicular to the compressive forces. During the beginning stage, some defects are formed around the indenter as shown in Fig. 5a, and then mainly median cracks with a minor crush zone beneath the indenter are formed and propagated downward with the tensile failure mode (Fig. 5a, b), which is developed under the increased loading condition of the rock sample as shown in Fig. 7 between point (a) and (b) where the letters (a)–(d) correspond to the letters (a)–(d) associated with the snapshots shown in Figs. 5 and 6. After the peak load, the radial cracks are initiated and propagated with the more expended crush zone (Fig. 5b, c) as shown in Fig. 7, point (b), (c). During the formation of the crush zone, volumetric

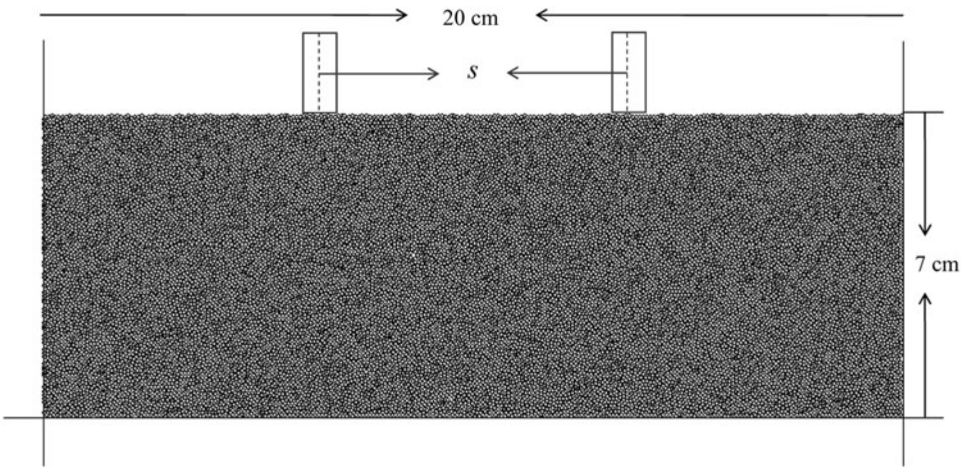

Fig. 3 Sample dimensions for the multi-indentation test; 20 cm width with 7 cm height; *s* is spacing between two indenters

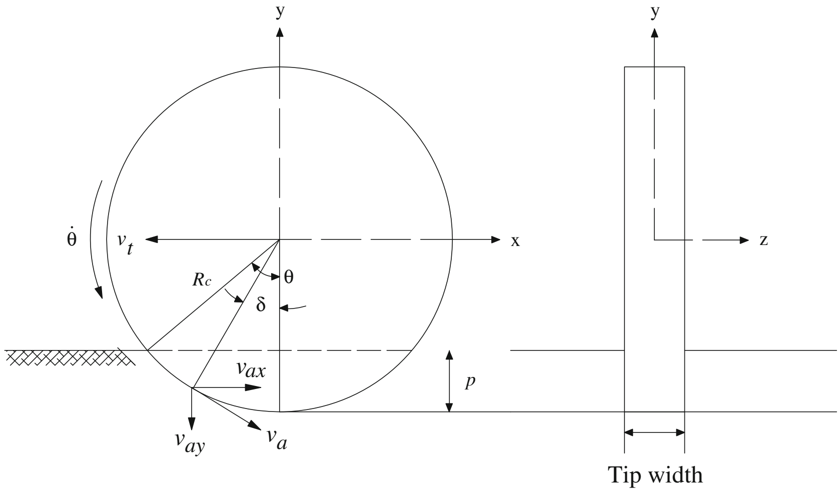

Fig. 4 Schematic view of disc cutter illustrating each velocity and geometric component. Shown quantities are θ: contact angle between the disc and rock sample at full penetration depth, $\dot{\theta}$: angular velocity, R_c: cutter radius, v_a: tangential velocity, v_t: translation velocity of disc cutter, δ: arbitrary angle at any contact point

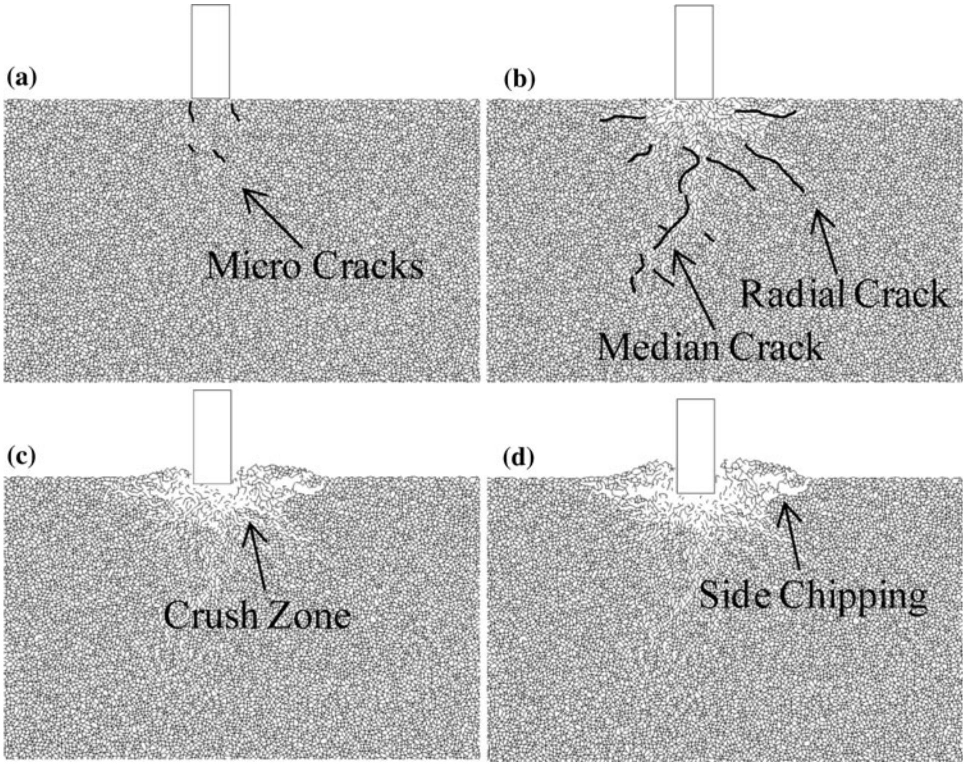

Fig. 5 The result of the simulation for rock fragmentation process induced by first indenter

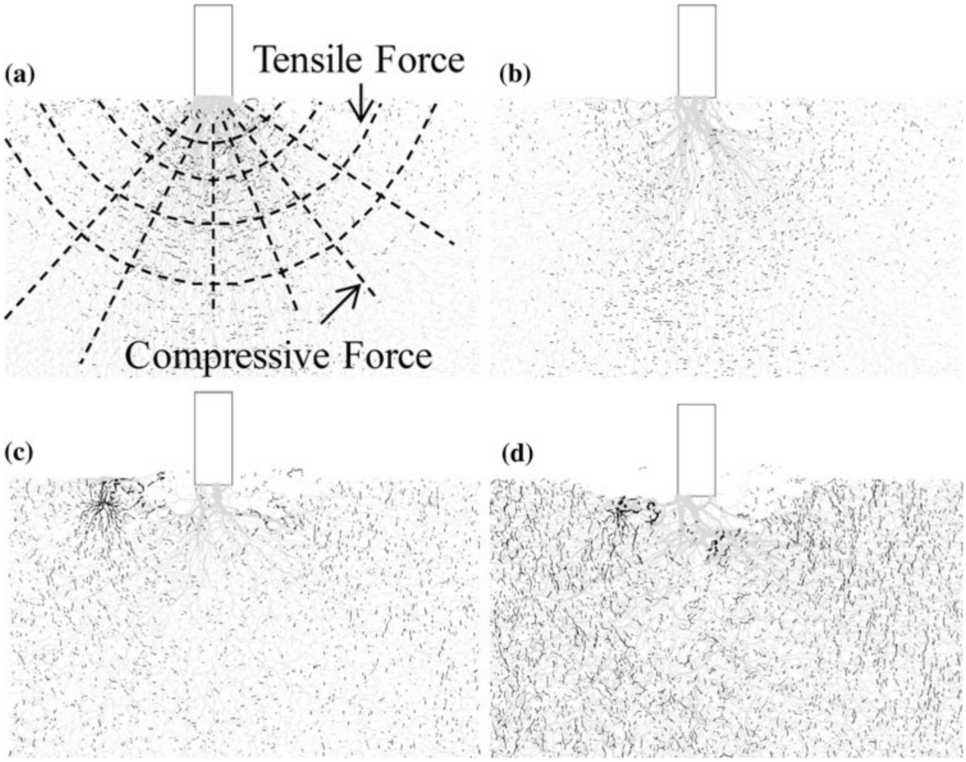

Fig. 6 The result of the simulation illustrating the internal forces: compressive (*gray color*) and tensile (*black color*) forces induced by first indenter

expansion takes place around the crush zone, which leads to a further tensile mode. As shown in Fig. 5d, the radial crack more clearly turns into a free surface such that small chipping is formed. At this stage, the velocity of the indenter is almost zero, and there are no significant reaction forces.

After completing the first indentation test, the second indentation test is successively implemented with a

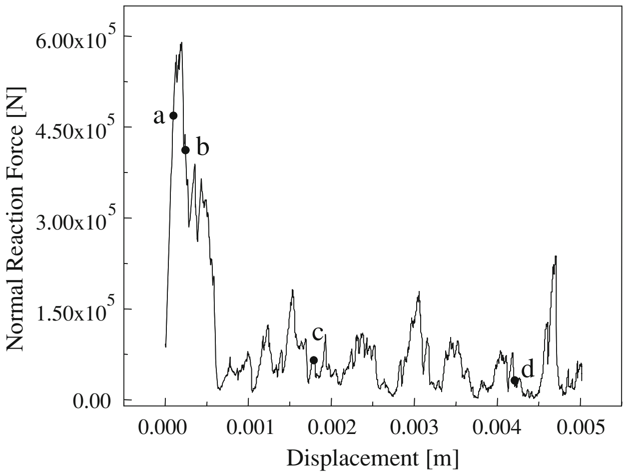

Fig. 7 Force-displacement graph induced by the first indenter

particular spacing. Figures 8 and 9 show a series of snapshots of the formation of crack systems and internal reaction forces for the second indentation. At the beginning stage shown in Fig. 9a, tensile and compressive reaction forces gradually increase under the indenter. Micro cracks are initiated around the indenter, as shown in Fig. 8a. As the penetration of the second indenter increases, median cracks are similarly initiated and propagated around the indenter (Fig. 8b). After the peak load as shown Fig. 10, point (b), the radial crack propagates further leftward with an approximately circular shape under the tensile failure mode (Fig. 8c, d). Therefore, a big chip is created between the indenters. In the final stage shown in Fig. 10, point (d), there are no significant reaction forces except the repeated peak-through behavior due to the collapse of the sample.

4 Measure of Specific Energy

A series of multi-indentation simulations are conducted with various *s/p* ratios for evaluating the optimal rock-cutting condition. Two different penetration depths, 4 and 5 mm, are used for tracing the variation of specific energy and also for comparing the optimized *s/p* ratio with the two different conditions. The result of the tests is summarized in Table 2.

The chipping formations under 4 mm penetration with various spacing ranging from 3 to 6.35 cm are shown in Fig. 11. The size of chipping varies according to the different spacing. Figure 11a shows an over-broken chip resulting from the narrow spaced cutters. Therefore, the specific energy becomes high and the efficiency of the cutting is low. When increasing the spacing to 4 cm, the required total energy is almost the same as the case of the 3 cm spacing, but the chipping area slightly increases without over-break. For the 5 cm spacing, the size of the chip increases, and the required total energy is increased as well (Table 2). For the 6.35-cm spacing shown in Fig. 11d, the main chipping between two indenters is not formed because of too largely spaced cutters; thus, a groove occurs. Overall, the minimized specific energy is obtained at the 4 cm spacing, and the optimum *s/p* ratio is about 10.

The variation of the total energy in terms of spacing shown in Fig. 12 illustrates that the total energy increases until a certain spacing, and then it is approximately constant, although the spacing increases. The optimum condition in general takes place around this inflection since a wider spacing than that of the inflection point does not provide a full chipping condition; instead, cracks are isolated around the indenters.

Fig. 8 The result of simulation for the rock fragmentation process induced by the second indenter

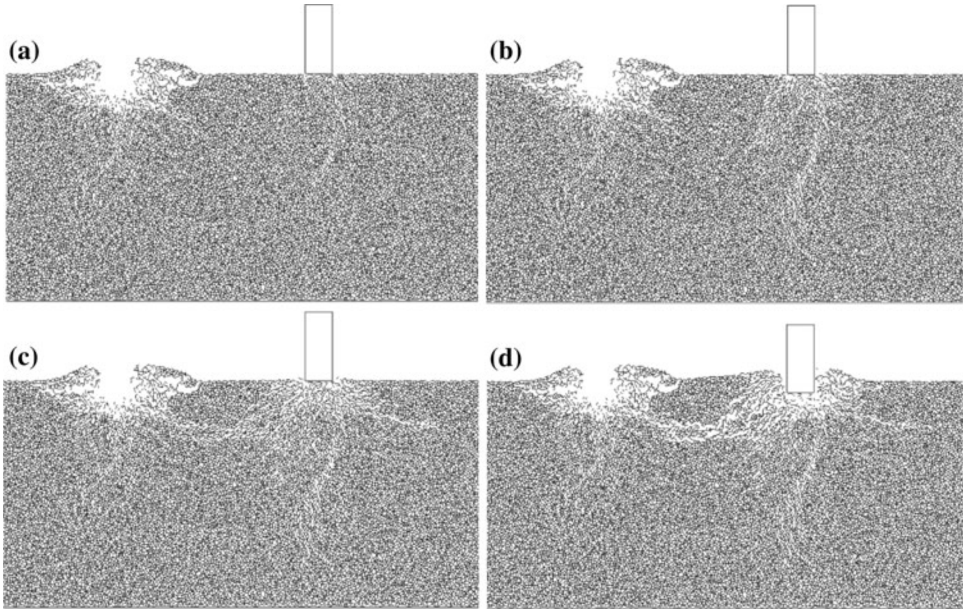

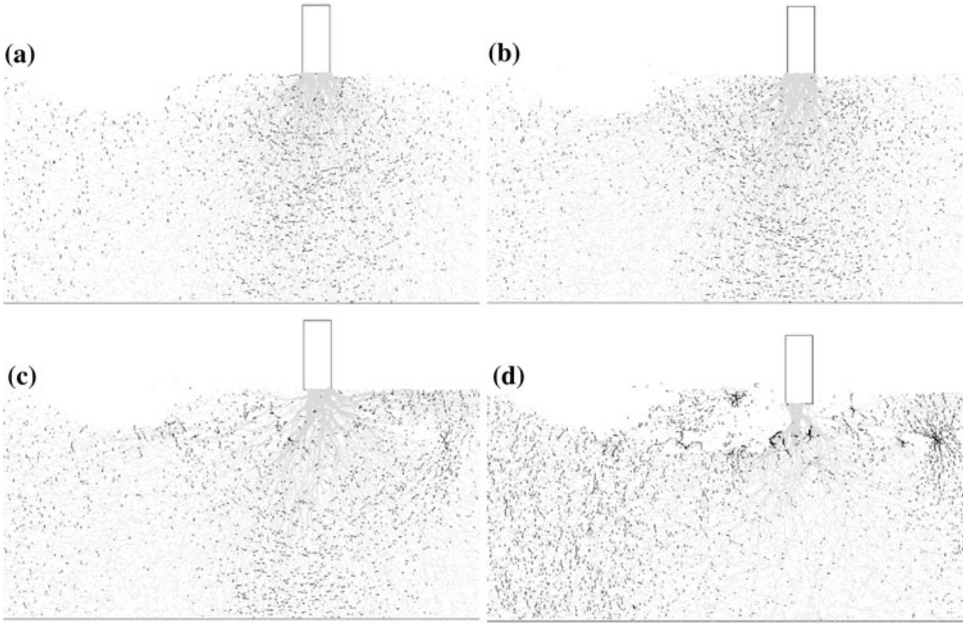

Fig. 9 The result of the simulation illustrating internal forces: compressive (*gray color*) and tensile (*black color*) forces induced by the second indenter

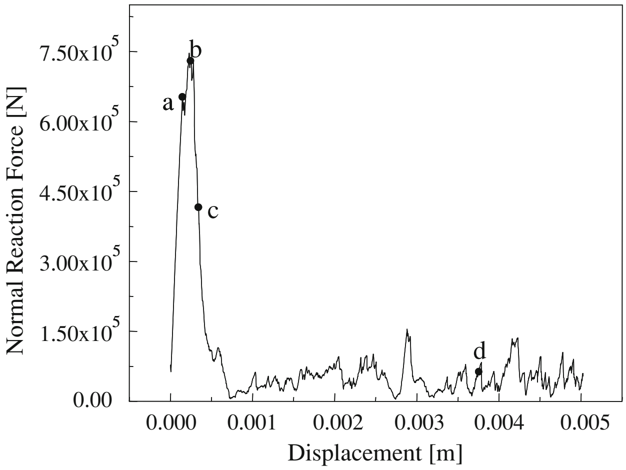

Fig. 10 Force-displacement graph induced by the second indenter

The relationship between the specific energy and the *s/p* ratio presented in Fig. 13 shows that the optimum *s/p* ratio is about 10–10.5 in both of the two different penetration depths. Thus, under fixed penetration conditions, a critical spacing exists; as penetration depth increases, the critical spacing tends to be increased such that the optimum *s/p* ratio provides an approximately constant value similar to the laboratory LCM test.

5 Parametric Study for Optimized *s/p* Ratio

A governing equation of the optimized *s/p* ratio is derived on the basis of the LEFM. Figure 14a shows a rock-chipping formation from the laboratory LCM test, and Fig. 14b presents a typical cross-sectional view of the rock chip having a longish circular shape under the optimal rock-cutting condition. A simplified general pattern of the optimized rock-cutting condition as shown in Fig. 15 would assume that the chip is favorably formed by a dominant single path with a circular shape to make a larger chip formation in terms of efficient energy usage.

When material properties and cutter geometry are constant, the chipping volume depends on the penetration depth. As the penetration becomes deeper, the optimized spacing would be larger with a similar chipping angle, α (Fig. 15b). Under the LEFM, the required energy per the optimal chipping area can be defined as

$$G_{IC} \propto \frac{F_c p}{r_c(2\alpha)(1m)} \tag{7}$$

where r_c shown in Fig. 15 is the chipping radius, $r_c = s/2\sin\alpha$ and F_c is a crack driving force. Equation 7 can be rearranged as a function of the *s/p* ratio such that the optimized chipping pattern is given by

$$\frac{s}{p} \propto \frac{F_c \sin\alpha}{2G_{IC}\alpha(1m)} \tag{8}$$

From a practical point of view, Eq. 8 is simplified as Eq. 9 since the range of the chipping angle observed from the result of the simulations and laboratory tests is approximately 10° to 40° such that the range of $\sin\alpha/\alpha$ is about 0.995–0.921, which is ignorable.

$$\frac{s}{p} \propto \frac{F_c}{G_{IC}(1m)} \tag{9}$$

Under the constant penetration depth, the optimized spacing is defined by F_c/G_{IC}. The unknown F_c related to

Table 2 Summary of the multi-indentation tests

Penetration (mm)	Spacing (cm)	Total energy (Nm)	Chip area (m^2)	Specific energy (Nm/m^2)	*s/p* ratio (dimensionless)
4.0	3.0	1,704	9.17×10^{-5}	1.86×10^{7}	7.5
4.0	4.0	1,704	1.14×10^{-4}	1.50×10^{7}	10.0
4.0	5.0	1,988	1.19×10^{-4}	1.66×10^{7}	12.5
4.0	6.4	1,953	Minor isolated chipping		15.9
5.0	4.0	1,736	7.35×10^{-5}	2.36×10^{7}	8.0
5.0	5.0	1,678	9.53×10^{-5}	1.76×10^{7}	10.0
5.0	5.5	1,905	9.72×10^{-5}	1.96×10^{7}	11.0
5.0	6.1	1,922	Minor isolated chipping		12.1

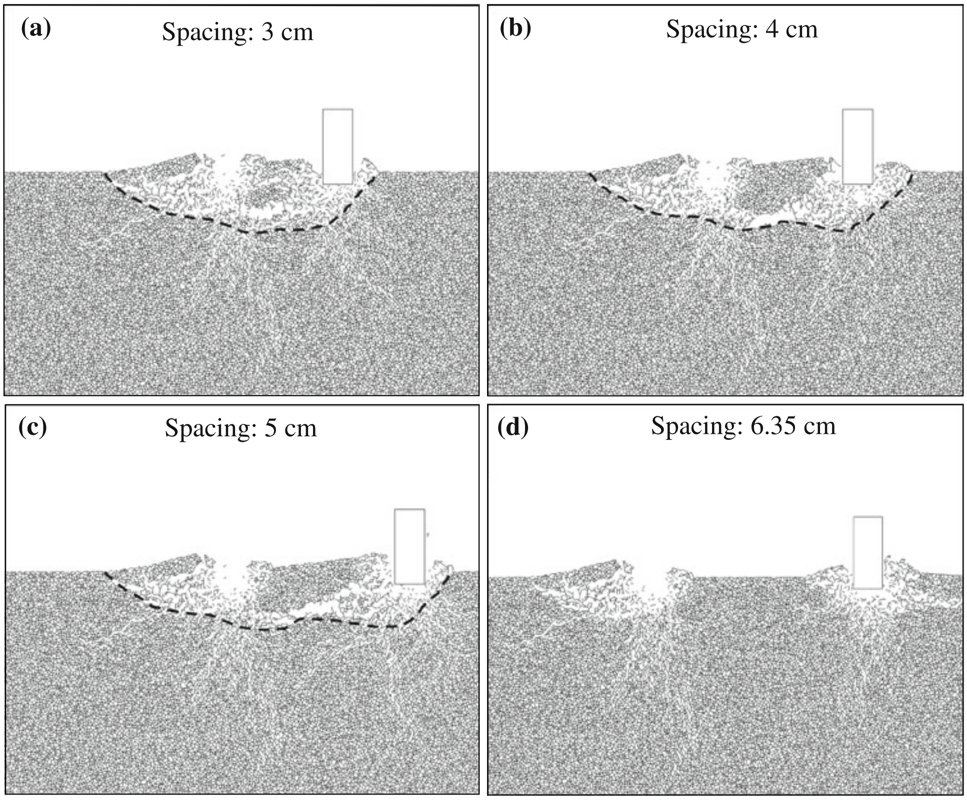

Fig. 11 Plots of multi-indentation tests for 0.004 m of penetration depth; dot line implies chipping area

the chipping formation is considered a function of major controlling parameters, σ_c, E and tip width, t, determined on the basis of indentation fracture mechanics (Swain and Lawn 1976). Thus, the controlling set of the parameters is given by

$$\left(\frac{s}{p}\right)G_{IC}\bigg/\left(\frac{\sigma_c^2}{E}t\right) = c \qquad (10)$$

where c is a constant and its value is also affected by the disc cutter geometry.

In order to validate Eq. 10, a series of multi-indentation simulations using the various material properties and different size of the disc cutters are performed. The detailed rock-cutting conditions including synthetic material properties are summarized in Table 3. The relation between the numerator and denominator of Eq. 10 is presented in Fig. 16, and the trend line is indicated by the dotted line with 78% correlation; R^2 and c is 1.17 for the simulated rock-like synthetic materials.

6 Application of Results and Discussion

Available rock-cutting data collected from literature resources (Roxborough and Phillips 1975; Snowdon et al. 1982; Cho et al. 2010) are applied to Eq. 10 for evaluating

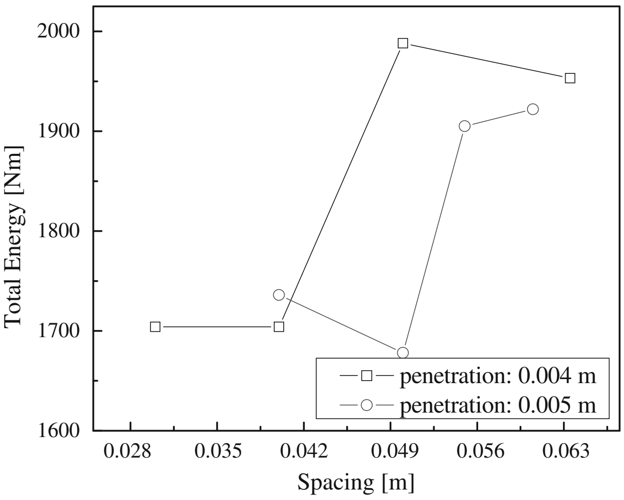

Fig. 12 Variation of total energy in terms of spacing

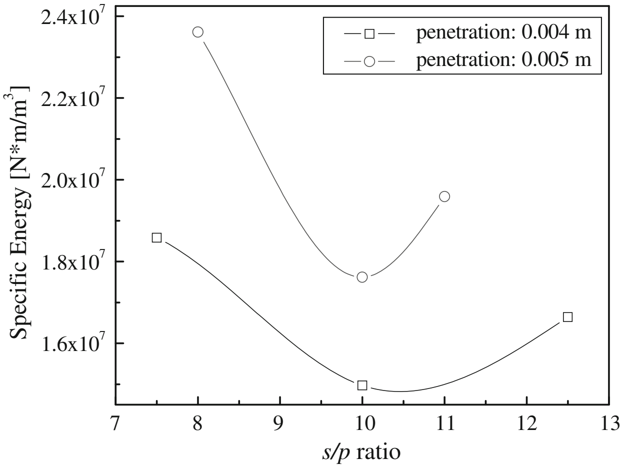

Fig. 13 Variation of total energy according to various *s/p* ratios

the performance of the proposed equation. The material properties and optimum *s/p* ratio are summarized in Table 4. The diameter of the disc cutter used was varied from 20 to 43 cm and Young's modulus, indicated by superscript star (E^*) in Table 4, is estimated by general representative values of the origin of rocks (Lama and Vutukuri 1978). Fracture toughness, K_{IC}, for converting to G_{IC} is estimated by using Zhang's formula (2002), applying a simplified relationship between the fracture toughness and the tensile strength. The suggested equation is given by

$$K_{IC} = 0.1453\sigma_t \quad \left(\mathrm{MPa}\sqrt{\mathrm{m}}\right) \tag{11}$$

The mechanical properties of the rock samples show a linear relation as shown in Fig. 17 with 0.14 of the coefficient and 68% of correlation, R^2, given by

$$\frac{s}{p} = 0.14\frac{\sigma_c^2 t}{EG_{IC}} \tag{12}$$

It is interesting to note that the coefficient on Eq. 12 is smaller than that on Eq. 10 calculated using the rock-like synthetic materials. This is hardly surprising given that inevitable limitations exist when the actual rock failure behavior is represented by the numerically synthetic materials by means of the conventional PFC2D (Diederich 2000; Potyondy and Cundall 2004; Cho et al. 2007). Generally, most intact rock shows that the ratio of compressive strength to tensile strength roughly ranges from 5–10. For synthetic materials used in the simulations, however, as indicated in Table 1, the ratio of compressive strength to tensile strength is 4.3. This low value of the coefficient results from the difficulty of developing the synthetic specimen from micro-properties to macro-properties on the one hand and the natural difference between actual rock and synthetic specimens, such as flaws and grain shapes of actual rocks, on the other hand, as described above researchers. Therefore, the higher coefficient in Eq. 10 is primarily a consequence of the lower strength ratio (σ_c/σ_t), but within the range of possible strength ratios of the rock.

By combining Eq. 4 into Eq. 12, a more simplified relation, Eq. 13, is obtained for the optimal *s/p* ratio and mechanical properties.

$$\frac{s}{p} = cB^2 t \tag{13}$$

where c is 0.14 of the coefficient, and B is material brittleness, as defined by Lawn and Marshall (1979), i.e.,

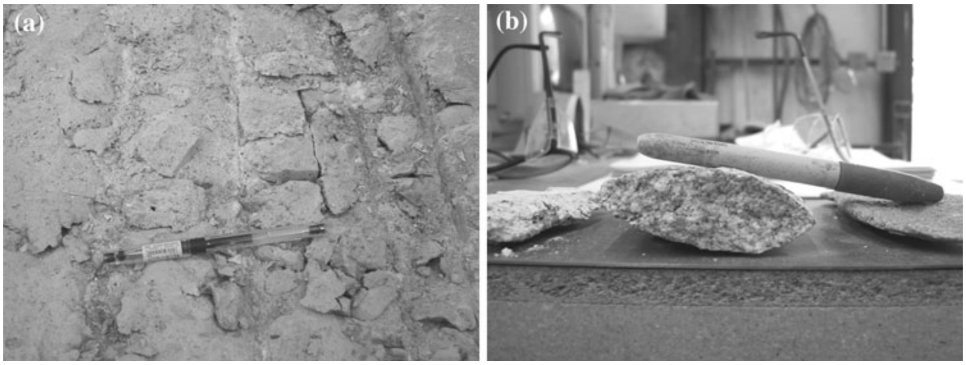

Fig. 14 The representation of **a** rock-chipping distribution after a real LCM test and **b** the typical chipping shape at optimal rock-cutting conditions

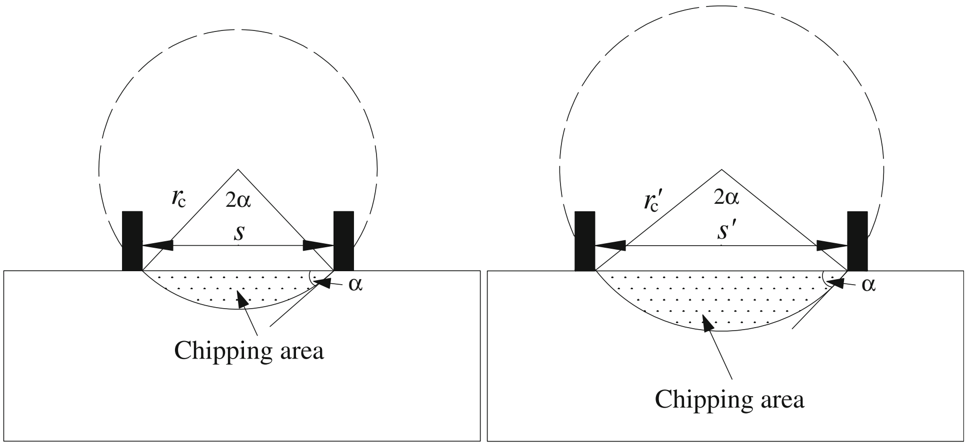

Fig. 15 Schematic representation of rock chipping under optimized rock-cutting conditions. r_c is chipping radius, s is spacing, and α is internal crack angle between indenters. **a** Shallow penetration, **b** deep penetration

Table 3 Measures of micro and macro material properties of synthetic materials including cutter dimensions for multi-indentation simulation

Micro material properties					Macro material properties				Cutter dimension	
μ	T_n (kN/m)	T_s (kN/m)	K_n (GPa)	K_s (GPa)	E (GPa)	v	σ_c (MPa)	G_{IC} (N·m/m^2)	R_c (m)	Tip width (mm)
0.5	15.8	31.6	30.0	7.5	8.74	0.24	28.4	97.1	0.06	8.4
1.0	15.8	31.6	30.0	7.5	8.74	0.24	29.0	90.8	0.06	8.4
1.0	15.8	31.6	60.0	15.0	17.4	0.24	27.6	54.3	0.06	8.4
0.5	31.6	63.2	30.0	7.5	8.86	0.24	58.2	262.1	0.06	8.4
0.5	31.6	31.6	30.0	7.5	8.82	0.24	44.8	213.2	0.06	8.4
0.5	7.9	31.6	30.0	7.5	8.62	0.25	15.6	27.2	0.06	8.4
0.5	23.7	47.4	120.0	30.0	34.4	0.24	43.1	132.1	0.06	8.4
0.5	39.5	79.0	40.0	10.0	11.5	0.24	70.5	400.9	0.06	8.4
0.5	15.8	31.6	30.0	7.5	8.74	0.24	28.4	97.1	0.1016	8.4
0.5	15.8	31.6	30.0	7.5	8.74	0.24	28.4	97.1	0.1016	13.0
0.5	15.8	31.6	30.0	7.5	8.74	0.24	28.4	97.1	0.2	8.4
0.5	15.8	31.6	30.0	7.5	8.74	0.24	28.4	97.1	0.1016	10.0
0.5	31.6	63.2	60.0	15.0	17.5	0.24	55.8	247.8	0.1016	8.4
0.5	7.9	15.8	60.0	15.0	17.2	0.24	14.0	14.9	0.06	10.0
0.5	23.7	47.4	40.0	10.0	11.6	0.25	46.1	172.1	0.06	10.0
0.5	31.6	63.2	10.0	2.5	3.04	0.26	66.7	845.9	0.06	10.0

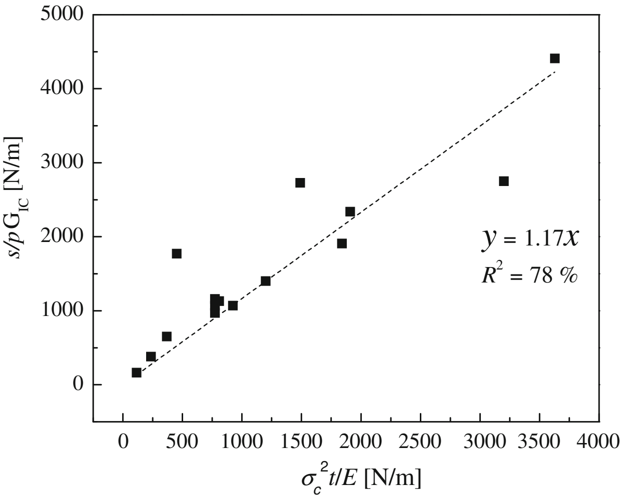

Fig. 16 Plot of Eq. 10 from the results of numerical simulations

$B = H/K_{IC}$, where H is material hardness quantified by the resistance of a material to plastic deformation given by $H = F_t/A$, where F_t is a peak load, and A is a contact area of indenter. The material hardness of the indentation analysis is conceptually comparable to the compressive strength of rock mechanics. Thus, Eq. 13 indicates that the more brittle rock material and the thicker disc tip width lead to a higher optimal *s/p* ratio. The thicker disc tip width of course demands a higher thrust force. Although some simplifications are involved in Eq. 13, the governing equation in terms of brittleness and tip width is applicable for estimating the optimal rock-cutting condition. A further study of the cutting process with the actual cutter shape and mechanical conditions such as pre-conditioning of the rock sample is desirable in conjunction with extensive experimental data.

Table 4 Rock properties used for LCM test and optimized *s/p* ratio

Rock	σ_c (MPa)	σ_t (MPa)	Optimum *s/p*	*E* (GPa)	K_{IC} (MPa$\sqrt{}$m)	G_{IC} (N·m/m^2)	References
Bunter sandstone	49.2	2.6	7	10.3^{*}	0.38	14.34	Roxborough and Phillips (1975)
Dolerite	340.0	27.5	12	110.0*	4.00	145.15	Snowdon et al. (1982)
Merrivale granite	174.0	10.0	10	42.6*	1.45	49.56	
Plas Gwilym limestone	155.0	13.7	15	63.6*	1.99	62.30	
Gregory sandstone	50.0	3.5	10	13.4*	0.51	24.94	
Macheon granite	108.0	10.4	13	71.0	1.33	24.9	Cho et al. (2010)
Hudong granite	91.0	12.3	12	47.3	1.13	27.0	
Sungnam gneiss	92.0	15.2	13	75.3	1.5	29.9	
Paldang gneiss	124.0	13.8	14	44.4	1.1	27.3	
Yeongwol limestone	64.0	8.9	15	77.3	1.16	17.4	
Busan granite	36.0	4.7	16	14.6	0.36	9.4	
Busan tuff	115.0	25.2	17	43.9	1.47	49.2	

(Note: *E** indicates a general representative value, and *t** is assumed to be 1 cm)

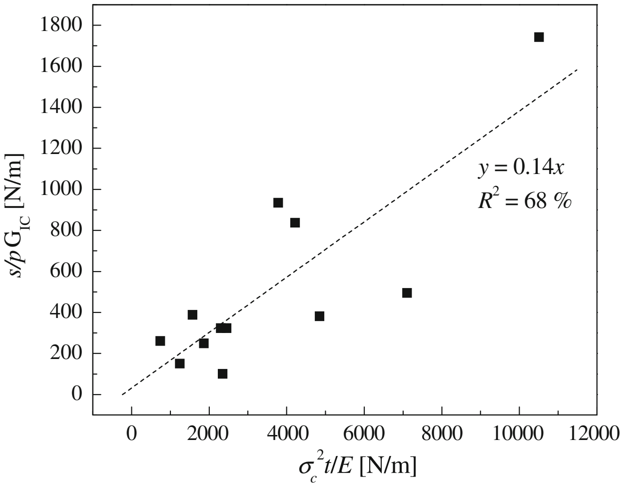

Fig. 17 Plot of Eq. 13 from the results of laboratory LCM tests

7 Conclusions

Multi-indentation tests for simulating the LCM test were used for investigating the process of rock fragmentation and finding the optimized *s/p* ratio in conjunction with intact rock properties through the use of the discontinuum code. The indentation tests were executed sequentially for representing the LCM test.

The rock fragmentation process performed by multi-indentation tests under the varied loading conditions with no confining stresses to represent proper boundary conditions of the laboratory LCM test showed similar crack formations and patterns with the experimental results from real LCM tests; initially the crush zone is formed beneath the indenter; then median cracks are initiated and propagated, while the reaction forces of the rock sample increase. After the peak load, radial cracks are formed with the expanded crush zone. During the second indentation simulation, the radial cracks are further propagated to the previous damaged zone induced by the first indentation. Therefore, a big chip is generated between two indenters. However, certain more widely spaced indenters than the critical spacing could not form a big chip; instead, the cracks are isolated near the indenters and form a groove. In such a case, a higher penetration depth is required for the formation of the full chipping condition. Thus, this result provides confidence that the numerical simulation performed here can be a useful tool to study the optimal rock-cutting conditions in terms of various rock properties and rock-cutting conditions.

The parametric study of the multi-indentation simulations indicates that there is a linear relationship between the optimal *s/p* ratio and mechanical properties, σ_c^2/EG_{IC}, which turned out to be $(\sigma_c/K_{IC})^2$ defining the square of the material brittleness, B^2. Therefore, the implications of this study for disc-cutting performance are that the optimized *s/p* ratio is mostly governed by material brittleness and cutter tip width.

References

Cho N, Martin CD, Sego DC (2007) A clumped particle model for rock. Int J Rock Mech Min Sci 44:997–1010

Cho JW, Jeon S, Yu SH, Chang SH (2010) Optimum spacing of TBM disc cutters: a numerical simulation using the three-dimensional dynamic fracturing method. Tunn Undergr Space Technol 25:230–244

Cook NGW, Hood M, Tsai F (1984) Observations of crack growth in hard rock loaded by an indenter. Int J Rock Mech Min Sci Geomech Abstr 21:97–107

Diederich MS (2000) Instability of hard rock masses: the role of tensile damage and relaxation. PhD thesis, University of Waterloo

Gertsch R, Gertsch L, Rostami J (2007) Disc cutting tests in Colorado red granite: implications for TBM performance prediction. Int J Rock Mech Min Sci 44:238–246

Gong QM, Jiao YY, Zhao J (2006a) Numerical modeling of the effects of joint spacing on rock fragmentation by TBM cutters. Tunn Undergr Space Technol 21:46–55

Gong QM, Zhao J, Hefny AM (2006b) Numerical simulation of rock fragmentation process induced by two TBM cutters and cutter spacing optimization. Tunn Undergr Space Technol 21:263

Griffith AA (1921) The Phenomena of rupture and flow in solids. Philos Trans Roy Soc Lond Ser A Containing Papers Math Phys Character 221:163–198

Huang H (1999) Discrete element modeling of tool-rock interaction. Ph.D thesis, University of Minnesota

Itasca Consulting Group Inc (1999) PFC2D Particle flow code computer manuals

Lama RD, Vutukuri VS (1978) Handbook on mechanical properties of rocks (Testing techniques and results—volume II). Trans tech publications

Lawn BR, Marshall DB (1979) Hardness, toughness and brittleness: an indentation analysis. J Ceram Soc 62(78):347–350

Lawn BR, Swain MV (1975) Microfracture beneath point indentations in brittle solids. J Mat Sci 10:113–122

Liu HY, Kou SQ, Lindqvist PA, Tang CA (2002) Numerical simulation of the rock fragmentation process induced by indenters. Int J Rock Mech Min Sci 39:491–505

Moon T, Nakagawa M, Berger J (2007) Measurement of fracture toughness using the distinct element method. Int J Rock Mech Min Sci 44:449–456

Potyondy DO, Cundall PA (2004) A bonded-particle model for rock. Int J Rock Mech Min Sci 41:1329–1364

Potyondy DO, Cundall PA, Lee CA (1996) Modelling rock using bonded assemblies of circular particles. In: 2nd North American Rock Mechanics symposium 1937–1944

Rostami J, Ozdemir L (1993) A new model for performance prediction of hard rock TBMs. Proc RETC Boston, MA, pp 793–809

Roxborough FF, Phillips HR (1975) Rock excavation by disc cutter. Int J Rock Mech Min Sci Geomech Abstr 12:361–366

Snowdon RA, Ryley MD, Temporal J (1982) A study of disc cutting in selected British rocks. Int J Rock Mech Min Sci Geomech Abstr 19:107–121

Swain MV, Lawn BR (1976) Indentation fracture in brittle rocks and glasses. Int J Rock Mech Min Sci Geomech Abstr 13:311–319

Teale R (1965) The concept of specific energy in rock drilling. Int J Rock Mech Min Sci Geomech Abstr 2:57–73

Yarema S, Krestin GS (1966) Determination of the modulus of cohesion of brittle materials by compressive tests on disc specimens containing cracks. Soviet Materials Sci 2(1):7–10

Yoon J (2007) Application of experimental design and optimization to PFC model calibration in uniaxial compression simulation. Int J Rock Mech Min Sci 44:871–889

Zhang ZX (2002) An empirical relation between mode I fracture toughness and the tensile strength of rock. Int J Rock Mech Min Sci 39:401–406